

## Detecting dynamical boundaries from kinematic data in biomechanics

Shane D. Ross,<sup>1</sup> Martin L. Tanaka,<sup>2</sup> and Carmine Senatore<sup>1</sup>

<sup>1</sup>*Engineering Science and Mechanics, Virginia Tech, Blacksburg, Virginia 24061, USA*

<sup>2</sup>*Department of Orthopaedic Surgery, Wake Forest University, Winston-Salem, North Carolina 27157, USA*

(Received 1 September 2009; accepted 2 November 2009; published online 5 January 2010)

Ridges in the state space distribution of finite-time Lyapunov exponents can be used to locate dynamical boundaries. We describe a method for obtaining dynamical boundaries using only trajectories reconstructed from time series, expanding on the current approach which requires a vector field in the phase space. We analyze problems in musculoskeletal biomechanics, considered as exemplars of a class of experimental systems that contain separatrix features. Particular focus is given to postural control and balance, considering both models and experimental data. Our success in determining the boundary between recovery and failure in human balance activities suggests this approach will provide new robust stability measures, as well as measures of fall risk, that currently are not available and may have benefits for the analysis and prevention of low back pain and falls leading to injury, both of which affect a significant portion of the population. © 2010 American Institute of Physics. [doi:10.1063/1.3267043]

**The identification of frontiers between qualitatively different kinds of behavior in a dynamical system is important in many applications. Increasingly, systems of interest are determined not by analytically defined model systems, but by noisy time series data sets resulting from experiments or complex simulations. Recently, the concept of Lagrangian coherent structures (LCSs), ridges in the state space distribution of finite-time Lyapunov exponents (FTLEs), has been used to locate these dynamical boundaries. The current approach to finding these structures requires a vector field in the state space at each instant in time. In this paper, we demonstrate a method that uses only trajectories reconstructed from time series. To demonstrate this approach, we analyze problems in musculoskeletal biomechanics, considered as exemplars of a class of experimental systems that contain boundaries which have gone largely ignored, despite their importance for determining possible behaviors and the relationship between them.**

### I. INTRODUCTION

A challenging and fundamental goal that remains in dynamical systems theory is to find dynamical structure in realistic systems of interest, systems defined not only by analytical models but also systems given by noisy data from experiments or large-scale simulations. The goal of finding structure fits into the larger context of phase space transport, a unified mathematical description of dynamical processes which can be applied to a wide range of physical phenomena across many scales.<sup>65,9</sup>

In the phase space transport problem, one identifies frontiers between regions of qualitatively different behavior, e.g., a boundary separating safety and failure regions of a mechanical or biomechanical system, as depicted schematically in Fig. 1(a). We contend that the locations of these boundaries or separatrices can be found by extracting information contained within time series data from observations obtained

from experiments. Rather than finding an average value of the Lyapunov exponents over phase space, as traditionally done in time series analysis, one can generate a Lyapunov exponent field, quantifying the trajectory sensitivity at different phase space locations, as shown in Fig. 1(b). This perspective can lead to a more thorough understanding of possible system behaviors, as the sensitivity field is used to identify phase space boundaries.

While the determination of separatrices is well developed for some domains, such as analytically known models of low dimensionality, there are many other domains where dynamical boundary identification will be fruitful, but has yet to be tried. Data-rich areas like biology, climate, and economics hold great potential.

In this paper, we focus on examples from musculoskeletal biomechanics, specifically the study of human balance control while sitting, standing, or walking. We demonstrate the possibility of determining a “threshold of stability” or recovery envelope—the set of states separating balanced states from falling states, that is, the boundary of a basin of stability—from experimental time series data.<sup>58,61</sup> Specifically, we find separatrices in time series data as ridges of a sensitivity field, as depicted in Fig. 1(b). Although one-dimensional ridges in a two-dimensional phase space are shown, the concept generalizes to higher dimension, where the ridge corresponds to a codimension one manifold in phase space. Previous research on time series analysis has focused on determining whether the dynamics comes from chaotic deterministic processes or noise.<sup>11,16,48</sup> But there is more information to be found in the data—namely, the structure and interconnectedness of the phase space as determined by boundaries between qualitatively different kinds of behavior.

To find behavioral boundaries, we borrow techniques originally developed for the analysis of fluid flows.<sup>28,24–27,52,38</sup> LCSs (Ref. 28) are phase space boundaries which are defined as the local maxima (technically, ridges) in

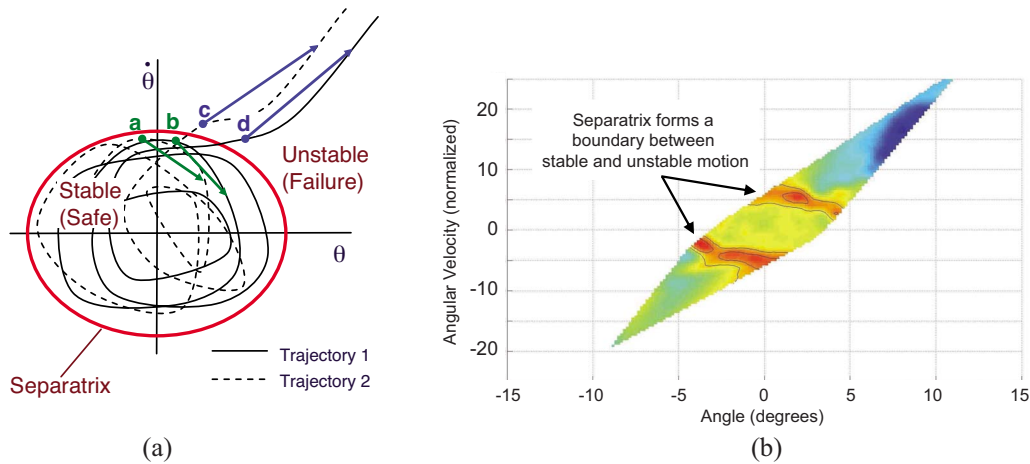


FIG. 1. (Color online) Detecting dynamical boundaries from measured data. (a) Schematic showing two example trajectories, both of which start in the stable region and end in the unstable region. By analyzing the motion of points along the trajectory appropriately, we can find the boundary or recovery envelope between stable and unstable (i.e., failure) motions. The divergence between two points (b and c) on opposite sides of a recovery envelope separatrix is larger than the divergence of points on the same side [pairs (a, b) and (c, d)], which tend to move together over short times. (b) An observable separatrix forms from simulated experimental trials of the wobble chair. The separatrix is found as a LCS, i.e., a ridge in the FTLE field.

a particular example of a sensitivity field: the FTLE field.<sup>52,38</sup> In general, LCSs are found by generating a FTLE field from phase space trajectories of the system, the first step in the boxed portion of Fig. 2. The trajectories are usually obtained by numerically flowing initial conditions under the numerically or analytically known vector field of the system, e.g., fluid flows inferred from particle image velocimetry (PIV). However, in many experimental settings, such as musculoskeletal biomechanics, only a few measured variables are produced (see Fig. 2), not the underlying dynamical vector fields which generate the measurements. Furthermore, it is sometimes the case that one can only measure the sensitivity of some subset of variables with respect to some other subset, which technically would not fit within the existing LCS framework, but which evidence suggests still can reveal important dynamical boundaries.<sup>57</sup>

Separatrices found via LCS methods have previously been used to analyze a handful of nonfluid dynamical systems, including analytical chemical models<sup>1</sup> and low degree of freedom (DOF) mechanical systems.<sup>13</sup> But little work has been done to determine phase space boundaries from experimental time series data.<sup>61,58</sup> Musculoskeletal biomechanical experiments commonly generate data in this form, that is, measured time histories of configuration space variables, e.g., position and orientations of various limbs.

A few examples of biomechanical systems are described below, along with hypotheses regarding dynamical boundaries.

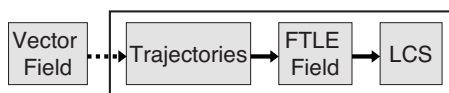


FIG. 2. Flowchart depicting how separatrices (as LCSs) are traditionally determined. The underlying vector fields are unavailable in musculoskeletal experiments; only the resulting time series (i.e., trajectories) are available. Therefore we must consider an algorithm that starts with trajectories (the boxed steps) while assuming that trajectories were generated by a, perhaps unknown, vector field.

### A. Balance recovery: Standing and falling

In biomechanics, a separatrix or recovery envelope exists between standing and falling, i.e., standing with postural sway is a distinctly different type of motion from falling. During standing, the body remains in the vicinity of an equilibrium position and may be characterized as dynamically stable over a suitable finite-time horizon. Compare this motion to falling where the body rapidly diverges from the vicinity of the equilibrium position at an increasing velocity. If one allows an experimental subject to take a step during fall recovery, another boundary will develop. Now three states exist: standing, recovering from a fall with one step, and falling. Each type of motion is divided from the other by a separatrix. Extending this idea, a state space diagram with multiple fronts may be generated.

Studies of bipedal stability date back at least 40 years with the conception of the zero moment point finding applications in walking robots.<sup>64,63</sup> Other studies have investigated the range of forward and backward lean that can be attained while maintaining an upright posture without stepping.<sup>67,40,35</sup> These studies considered the system to be quasistatic where stability is controlled by muscle strength, base of support, and the location of the center of mass (COM). By analyzing the results of these studies, a stable region may be defined in one state space dimension (position) based on the above parameters. Pai *et al.* expanded this work to two dimensions by including velocity in his mathematical models<sup>45,30</sup> but only a small portion of state space was evaluated. Yang, Pai, and others investigated the contribution of velocity for maintaining balance during gait.<sup>70,72,71</sup> With the exception of Pai's work, previous work has considered the separatrix in the configuration space rather than (correctly) in the state space; a conceptual problem which has been dealt with in related work on transition state theory in both chemistry and celestial mechanics contexts.<sup>34,31,21,19,9,10,20</sup>

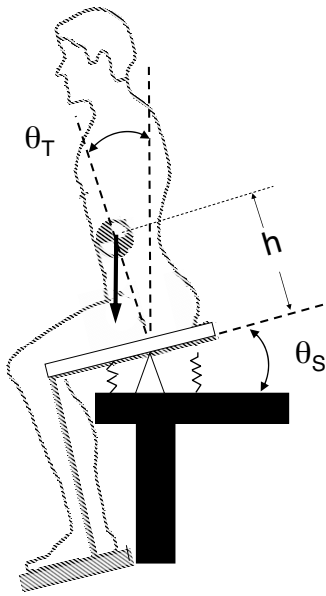


FIG. 3. The wobble chair is an unstable sitting apparatus designed to isolate the movement of the low back to determine torso stability. (Figure is adapted from Fig. 1 in Ref. 6 and Fig. 1a in Ref. 57.) The angle  $\theta_s$  is the angle the seat makes with the horizontal and  $\theta_T$  is the angle the torso makes with the vertical.

### B. Torso stability: Assessed with wobble chair

A comparable problem to balance recovery in standing postural sway is the challenge of maintaining torso stability. In this case, a separatrix exists delineating stable torso sway from unstable and potentially injurious motion. One can study torso stability using an experimental apparatus known as the wobble chair, shown schematically in Fig. 3. Torso stability is necessary to avoid large deformations in the lumbar spine and its loss is often associated with low back injury and pain.<sup>22,5</sup> We propose to extract this separatrix from experiments. Preliminary results from a reduced order model which captures the essential features of the experimental data suggest this is possible.

### C. Stability in walking versus falling

The computation of FTLEs from experimental data has been used before in musculoskeletal biomechanics, particularly to quantify local dynamic stability during locomotion.<sup>12</sup> However, separatrices between dynamically stable walking/running can also be evaluated using the methods proposed herein.

For example, a boundary or frontier exists in state space between stable walking and falling, as shown in Fig. 4 (preliminary results in Ref. 43). During walking, the body remains within a certain limited domain of state space and may be characterized as locally dynamically stable. Beyond this stable region, dynamic stability cannot be maintained by simply making minor corrections to the step length, gait speed, or foot location.

We suggest that the identification of this boundary, the recovery envelope, is critical to the assessment of fall risk. We hypothesize that an individual's risk can be measured by considering how close in phase space his trajectory comes to

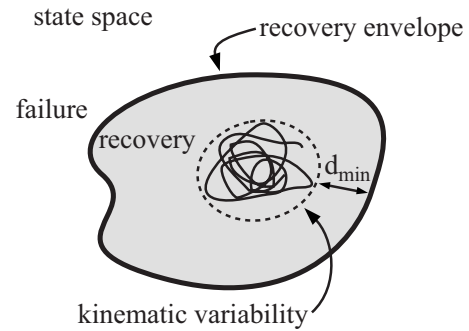


FIG. 4. Recovery envelopes: a new tool in the evaluation of fall risk. Shown schematically, the boundary between the states corresponding to stable walking (recovery) and falling (failure) is given by a recovery envelope (thick line). We assume the state space is equipped with a metric and suggest that the minimum state space distance between a subject's kinematic variability and their recovery envelope ( $d_{\min}$ ) can be used as a measure of their falling risk.

his recovery envelope, as depicted schematically in Fig. 4. This framework provides a means to quantify the effects of various factors on fall risk (age of individual, load weight, and distribution) as well as the effectiveness of training on reducing fall risk.

### D. Organization of paper

In this paper, we develop a framework for the detection of dynamical boundaries and, where appropriate, phase space transport related to those boundaries, in the field of musculoskeletal biomechanics. Although biomechanics is our focus, we consider the methods applicable to a larger class of amenable observational and experimental systems. The organization of the paper is as follows. The mathematical analysis tools used to detect dynamical boundaries from data are described in Sec. II; in particular, we describe a new extraction and characterization algorithm. In Sec. III, we describe some models and experiments for postural stability with particular attention to the wobble chair, an experimental apparatus used to obtain postural data. One and two DOF models are described and their dynamical boundaries analyzed using the novel extraction and characterization procedure. A recent effort to extract the basin of stability volume from experimental data is also summarized. Finally, in Sec. IV we provide some concluding comments and directions for future development and speculate on the use of measured recovery envelopes as a new tool in risk assessment.

## II. DETECTING DYNAMICAL BOUNDARIES

### A. Sensitivity analysis and the finite-time Lyapunov exponent field

In this section, we briefly review some mathematical preliminaries regarding sensitivity of trajectories (following, e.g., Refs. 46 and 66). Suppose we are given a reference trajectory  $x(t)$  through phase space going from  $x_0$  at time  $t_0$  to  $x_1$  at time  $t_1$ . Although the phase space for most mechanical systems is a non-Euclidean manifold (e.g., a tangent bundle of a configuration space), we assume that the effect on measuring sensitivity is negligible and therefore take our

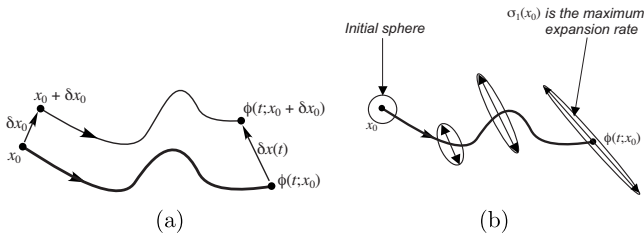


FIG. 5. (a) A trajectory  $\phi(t; x_0)$  and a neighboring trajectory  $\phi(t; x_0 + \delta x_0)$ . (b) The state transition matrix is a deformation gradient about the reference trajectory describing how an initially spherical blob of surrounding states deforms into an ellipsoid.

phase space as Euclidean (which has some justification; see, e.g., Ref. 37). We assume the trajectory evolves under the dynamical equations of a time-independent (autonomous) system in first-order form,

$$\dot{x} = f(x), \quad x \in \mathbb{R}^n. \tag{1}$$

This equation describes a vector field. The sensitivity of the reference trajectory is discussed below.

Let trajectories of the system (1) with  $x(t_0) = x_0$  be denoted by  $\phi(t; x_0)$ . In other words, the object  $\phi: \mathbb{R} \times \mathbb{R}^n \rightarrow \mathbb{R}^n$  denotes the flow map of the dynamical system (1), mapping a state  $x_0$  along its trajectory to the resulting state  $x$  at time  $t$ .

Consider a second trajectory that starts slightly away from the reference trajectory  $\phi(t; x_0)$ , i.e., starts from the perturbed initial vector  $x_0 + \delta x_0$  at time  $t_0$ . As the trajectories evolve, the vector displacement (or perturbation vector)

$$\delta x(t) = \phi(t; x_0 + \delta x_0) - \phi(t; x_0) \tag{2}$$

will also evolve, as illustrated in Fig. 5(a). For our purposes, the “second trajectory” might be the result of another experimental trial or another portion of the same trajectory separated by a sufficient amount of time to avoid a substantial autocorrelation.

The linear relationship between small initial perturbations and perturbations at some time  $t$  is

$$\delta x(t) = \Phi(t; x_0) \delta x_0, \tag{3}$$

where  $\Phi(t; x_0) = \partial \phi(t; x_0) / \partial x_0$  is the  $n \times n$  state transition matrix (also known as the fundamental matrix; see, e.g., Ref. 46). The state transition matrix can be viewed as a deformation gradient in the phase space [see Fig. 5(b)]. The matrix  $\Phi(t; x_0)$  contains information about expansion and contraction as well as the rotation of an initially small collection of states, starting near  $x_0$ , due to the locally deforming nature of the flow. Taking the vector norm on  $\mathbb{R}^n$  of Eq. (3), the size of the final perturbation vector at time  $t$  is given by

$$\|\delta x(t)\| = \sqrt{\delta x_0^* [\Phi(t; x_0)^* \Phi(t; x_0)] \delta x_0}, \tag{4}$$

where  $A^*$  denotes the transpose of the matrix  $A$ , and the perturbations are considered as column vectors. Within Eq. (4), we see the symmetric matrix

$$\Sigma = \Phi(t; x_0)^* \Phi(t; x_0), \tag{5}$$

which is the finite-time right Cauchy–Green deformation tensor.<sup>52</sup> The matrix  $\Sigma$  is a rotation-independent measure of deformation; it gives the square of the local change in dis-

tances due to deformation.<sup>62,18</sup> Since  $\Sigma$  is a symmetric, positive definite matrix, it has  $n$  real, positive eigenvalues.<sup>56,38</sup>

One can associate with the point  $x_0$  a maximum FTLE given by

$$\sigma(x_0) = \frac{1}{|T|} \ln \sqrt{\lambda_{\max}(\Sigma)}, \tag{6}$$

where  $T = t - t_0$  is the finite duration over which expansion is measured (i.e., the horizon time) and  $\lambda_{\max}(\Sigma)$  is the maximum eigenvalue of  $\Sigma$  with the corresponding (normalized) eigenvector  $\hat{e}_{\max}(x_0)$ .<sup>52</sup> In other words, if  $\delta x_0$  is along  $\hat{e}_{\max}(x_0)$  at time  $t_0$ , then maximum stretching occurs (over the horizon time) and the length of the perturbation vector becomes  $\|\delta x(t)\| = e^{\sigma(x_0)T} \|\delta x_0\|$ , where  $t = t_0 + T$ .

Each point  $x$  of the phase space has a FTLE value associated with it, effectively representing the stretching over a time  $T$  of a small portion of phase space centered at  $x$ , as in Fig. 5(b). Therefore, we refer to the object  $\sigma(x)$  as the maximum FTLE *field*, or more informally as the FTLE field (where the maximum FTLE is understood). It is important to emphasize that this is a scalar field rather than a single scalar value obtained by averaging over phase space. The FTLE field,  $\sigma: \mathbb{R}^n \rightarrow \mathbb{R}$ , can be viewed as a real-valued graph over the phase space. Topological features of this graph, in particular ridges, are interpreted as having dynamical significance as phase space transport barriers<sup>52</sup> which act as a skeleton organizing the overall phase space transport structure. Before we discuss how the ridges are extracted, we discuss how to obtain a FTLE field in the absence of an explicitly known vector field, i.e., in the absence of known evolution Eqs. (1).

## B. Generating the FTLE field from trajectories

We have developed a method to construct a FTLE field using only trajectory data.<sup>58</sup> This approach eliminates the need for the generating vector field, which is generally unavailable in a biomechanics environment. Typically in biomechanics experiments a finite number of body segments are tracked and stored as time series data. Some of these techniques include measuring of kinematic movement trajectories using (a) three-dimensional (3D) video motion analysis, (b) accelerometer data, (c) gyroscopic data, or (d) some combination.

### 1. State space reconstruction

Since the system under study is a mechanical system, we take the measured position and/or angular coordinates as a function of time ( $\theta(t)$ ) and numerically construct the time derivatives ( $\dot{\theta}(t)$ ). We take the  $n$ -dimensional space of  $x = (\theta, \dot{\theta})$  as the reconstructed state space.<sup>44,42,23</sup> However, we note that the method of using a FTLE field to find a separatrix is not tied to any particular means of state space reconstruction. For instance, time-delay reconstruction,<sup>15,32,50</sup> which is appropriate for both mechanical and nonmechanical systems, can also be used.

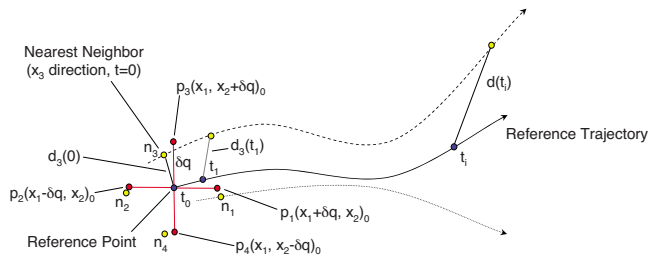


FIG. 6. (Color online) Estimating the maximum FTLE at a location in phase space by evaluating the growth of perturbation vectors in multiple state space directions. We make the assumption that the maximum FTLE dominates the evolution of the perturbation vectors.

**2. Calculating the FTLE field from discrete trajectory data**

The FTLE field is estimated as the rate of separation of neighboring trajectories. Traditionally, the FTLE for a location in state space is found by tracking the evolution of trajectories with initial locations defined by a regular grid.<sup>52</sup> However, when a vector field is not available, discrete data points near the reference point must be selected to estimate the local separation rate. In order to understand how this is determined from experimental time series data, consider the reference trajectory shown in Fig. 6. With a reference point established, a target location ( $p_1$ ) is identified that is a perturbation distance  $\delta q$  from the reference point in state space. The data point closest to  $p_1$  on another trajectory is then found,  $n_1$ . The other trajectory can be from either a different experimental trial or another portion of the same trial separated by a sufficient amount of time to avoid a correlation with the reference point over the horizon time. This process is repeated for other directions. Using this method,  $2n$  neighbors are found for each reference point corresponding to positive and negative directions of each dimension of state space. As multiple nearest neighbors are considered, perturbations are sampled in multiple state space directions which increase the likelihood of a detected separation lying in the direction of maximum expansion.

By treating each point in the time series as the reference point, a FTLE can be calculated for the regions of state space that are explored by the trajectories. A FTLE field may be generated by associating each FTLE value with the state space locations from which it was calculated. This approach differs from previous methods that averaged the FTLE over time and state space<sup>15,50,11.69</sup> to determine a single scalar value for the system.

**3. Modifying factors**

The two major factors influencing the estimate of the FTLE field are the choice of horizon time  $T$  and perturbation distance  $\delta q$ . In practice, one determines  $T$  heuristically by starting from zero and increasing  $T$  until the structure is observed.<sup>52</sup> In many applications the system of interest likely has a characteristic time scale that could be used. Regarding  $\delta q$ , we can view this distance as an important coarse-graining parameter selected to be large enough to overcome system noise, yet small enough to reveal local features of the FTLE field. Preliminary parameter sensitivity analysis shows this method to be relatively insensitive to the value of  $\delta q$ ;

that is, reductions in the value of  $\delta q$  by two orders of magnitude reduced the smoothness of the FTLE field, but did not change the locations of FTLE ridges. Further research is needed to establish the proper value of the coarse-graining parameter, e.g., what range of values is appropriate given a particular uncertainty environment (i.e., point cloud density or level of system noise?). However, separatrices computed from vector fields have been shown to be robust with respect to some kinds of noise.<sup>25,27</sup> Similarly, our work, described below in Sec. III, suggests the same is true for separatrices computed from individual trajectories, making them attractive for use in experimental data analysis where noise sensitivity is an important issue.<sup>4,14,17</sup>

**C. Extracting and characterizing boundaries from the FTLE field**

A systematic method for not only extracting—but also characterizing—dynamical boundaries or LCS is useful for tracking and identifying individual features that may merit further analysis. Once the FTLE field is available using the method described above, it can be analyzed as a height field. The problem of extracting LCS then becomes the detection of the ridges in this height field. For some systems, FTLE ridges can be determined by visual inspection of the field. For other systems, the FTLE can be very complicated, warranting automated methods. Different approaches have been used to highlight and illustrate ridges in FTLE fields; these methods focus on visualization of the ridge.<sup>39,53</sup> Here we adopt the method proposed by Ref. 51 where the ridges are detected and categorized in terms of their strength per unit length.

**1. LCS detection algorithm**

Consider initially a FTLE field over a two-dimensional phase space. A point  $x$  belonging to a one-dimensional ridge of the FTLE field has to satisfy the following set of equations:

$$\lambda_{\min}(x) < 0, \quad \nabla \sigma(x) \cdot \mathbf{v}_{\min}(x) = 0, \tag{7}$$

where  $\lambda_{\min}(x)$  is the minimum magnitude eigenvalue of the Hessian matrix  $\nabla^2 \sigma(x)$  with corresponding eigenvalue  $\mathbf{v}_{\min}(x)$ . These conditions can be interpreted as the first derivative in the direction transverse to the ridge axis is equal to zero (i.e., a local maximum/minimum) and the second derivative in the transverse direction is negative (i.e., the curvature is negative when the field is at a local maximum in the transverse direction). The conditions in higher dimension are given in Ref. 51. The algorithm for detecting and classifying a ridge consists of five steps: scale-space representation and ridge point detection, dynamical sharpening, connecting ridge points into ridge curves, choice of best scale, and classification of ridges (by, e.g., phase space barrier strength). The scale-space representation consists of a convolution of the function  $\sigma \in C^2(\mathbb{R}^2, \mathbb{R})$  with a Gaussian kernel  $g \in C^2(\mathbb{R}^2, \mathbb{R})$ ,

$$\sigma_a(x) = g(x; a) * \sigma(x), \tag{8}$$

where  $a$  determines the value of the *scale* and the Gaussian kernel  $g \in C^2(\mathbb{R}^2, \mathbb{R})$  is given by

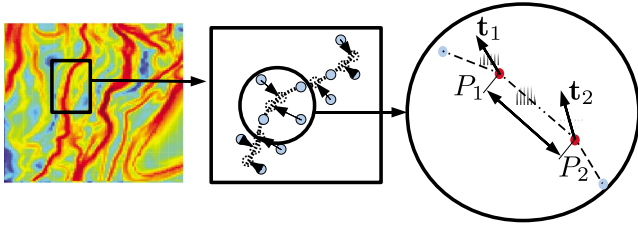


FIG. 7. (Color online) Main steps of the algorithm. From the FTLE field (left panel) the ridge points are calculated and aggregated toward the ridge axis (central panel). Thereafter, the points are appropriately connected (right panel) in order to create continuous curves.

$$g(x;a) = \frac{1}{2\pi a^2} \exp\left[-\left(\frac{|x|^2}{2a^2}\right)\right]. \tag{9}$$

This produces smoother images with the parameter  $a$  controlling the level of filtering. The points satisfying the ridge test conditions (7) are collected and they become the initial condition for the dynamical sharpening step. A ridge acts as an attractor for the gradient dynamical system,<sup>39</sup>

$$\frac{dx}{ds} = \nabla \sigma_a(x), \tag{10}$$

where  $s$  is the arc length along the gradient lines of  $\sigma_a(x)$ . The points accumulated along the ridge axis are then connected. Two points  $P_1$  and  $P_2$ , as in Fig. 7, belong to the same ridge if they satisfy the following conditions:

$$|P_2 - P_1| \leq d_0, \tag{11}$$

$$|\sigma_a(P_2) - \sigma_a(P_1)| \leq h_0, \tag{12}$$

$$\arccos\left(\frac{\mathbf{t}_2 \cdot \mathbf{t}_1}{|\mathbf{t}_2||\mathbf{t}_1|}\right) \leq \alpha_0, \tag{13}$$

$$\arccos\left(\frac{\mathbf{t}_1 \cdot (P_2 - P_1)}{|\mathbf{t}_1||P_2 - P_1|}\right) \leq \alpha_0, \tag{14}$$

where  $\mathbf{t}_1$  and  $\mathbf{t}_2$  are the eigenvectors corresponding to the maximum magnitude eigenvalues of the Hessian matrix  $\nabla^2 \sigma(x)$ , which are tangent vectors to the ridge at  $P_1$  and  $P_2$ , respectively. Equation (11) states that the two points must be closer than a threshold  $d_0$ . Equation (12) checks if the difference in height between the two points is lower than a threshold  $h_0$ . Equation (13) tests if the angle between  $\mathbf{t}_1$  and  $\mathbf{t}_2$  is smaller than  $\alpha_0$ . This comes from the assumption that the ridge curves are continuous and differentiable and therefore properties change smoothly throughout the curve, in particular, there should be no sharp corners to the curves. In practice, the values for  $(d_0, h_0, \alpha_0)$  are determined heuristically and may depend on  $a$ . Finally, Eq. (14) is a check on the alignment of the vector connecting  $P_1$  and  $P_2$  with the tangent vector at the point  $P_1$ . If these four conditions are satisfied points  $P_1$  and  $P_2$  are considered to be in the same ridge set, as illustrated in the right panel of Fig. 7.

Once the ridges have been detected they are classified based on the flux across them (following Ref. 52),

$$\frac{\mathbf{t} \cdot \nabla \sigma}{\mathbf{n} \cdot \nabla^2 \sigma \mathbf{n}} \left( \mathbf{t} \cdot \left( \frac{\partial \mathbf{n}}{\partial t} - J \mathbf{n} \right) \right), \tag{15}$$

where  $J$  is the Jacobian matrix of the velocity field and  $\mathbf{t}$  (respectively,  $\mathbf{n}$ ) are unit vectors which are tangent (respectively, normal) to the ridge at the evaluated ridge point. Since the velocity field is in general unavailable, only the first-order term of the flux equation (15) is used to measure the strength,

$$F \equiv \left| \frac{\mathbf{t} \cdot \nabla \sigma}{\mathbf{n} \cdot \nabla^2 \sigma \mathbf{n}} \right|. \tag{16}$$

The strongest ridges have  $F$  close to zero, considered both pointwise and as an average per unit length.

### III. SEPARATRICES IN MUSCULOSKELETAL BIOMECHANICS

#### A. Postural stability and the wobble chair

Postural stability is essential for biped walking and standing. In order to achieve an upright posture each component of the kinematic chain must be sufficiently stabilized. Critical components include the ankle, knee, hip, lumbar spine, and cervical spine. Loss of stability may result in falls, a leading cause of orthopedic injuries in the elderly which can begin a chain of medical complications often leading to death. In addition, falls account for at least 12% of all non-fatal injuries involving days away from work, and fall accidents account for 11.9% of occupational-related fatalities in the United States.<sup>3</sup> Furthermore, loss of stability in the lumbar spine has often been considered a contributing factor to low back injuries and pain. Low back pain is a common medical ailment afflicting 80% of the population at some time in their life.<sup>33,49</sup>

Mathematical models have been used to study postural stability during standing.<sup>47,67,2,7</sup> People generally use an ankle strategy to maintain stability during quiet standing.<sup>29,68,40</sup> For movement in the sagittal plane (forward and backward) the motion may be modeled as a planar inverted pendulum with control applied at the ankle joint. More complex systems that also take into account frontal plane motion (left and right) may be modeled as an inverted spherical pendulum, again with control applied at the ankles.

Spinal stability has been studied using an unstable sitting apparatus.<sup>6,36,54,61</sup> In these experiments the participant sits on the unstable seat and maintains rigidity of the body except for small movements of the lumbar spine. One such device, the wobble chair, consists of a seat supported by a central ball joint (Figs. 3 and 8). Attached to the seat is a leg rest to minimize relative movement within the lower body. Stabilizing springs located at the front, back, left, and right of the ball joint help support the seat.

#### B. One degree of freedom model

A one DOF planar inverted pendulum model is appropriate to simulate sagittal motion during quiet standing or a reduced order model of the planar wobble chair. In both systems torque is applied at the base to maintain the stability of the pendulum in the upright vertical position. The math-

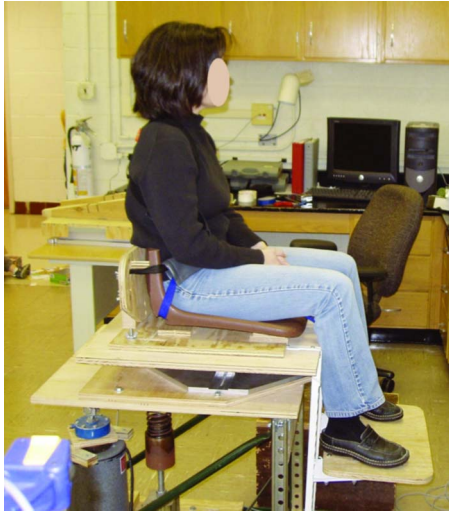


FIG. 8. (Color online) Subject balances on the wobble chair moving the lumbar region of her torso to maintain stability.

ematical model we describe is appropriate for both, but we use parameters applicable for the wobble chair.

**1. Sagittal plane standing**

During quite standing (no intentional movement), researchers often investigate motion within the sagittal plane only. This simplification is done to study the effects of neuromuscular control without the added complexity of 3D movement.

For the case of one DOF quiet standing, force is applied through the Achilles tendon to plantar flex (push down) the foot. When larger forces are applied, the center of pressure (COP) of the ground reaction force moves toward the front causing a torque about the ankle that accelerates the COM toward the rear. When small forces are applied, the COP shifts toward the rear and the COM accelerates toward the front. During this process the other major joints remain relatively fixed. Thus, control is applied at the ankle to maintain stability of what is essentially an inverted pendulum.

**2. Reduced order planar wobble chair**

In order to begin to understand the behavior of the full order system, a reduced order model was developed for the wobble chair (see Fig. 9). In the physical system, the body pivots at the lumbar spine (L4-L5), but in this model, motion is restricted to the sagittal plane and the angle between the lower body and upper body is fixed. These constraints imply that the difference between  $\theta_S$  and  $\theta_T$  is constant. We consider the dynamics of a single angle  $\theta$ , the angle from the pivot to the COM, measured from the vertical. Stabilizing springs like those used in the actual wobble chair are included in the model. In addition, a limited gain proportional-derivative control is incorporated which allows the system to have a stable equilibrium point at the upright vertical position. The existence of this stable region was observed in wobble chair experiments where participants were able to balance for 30 s in a statically unstable configuration.<sup>61</sup>

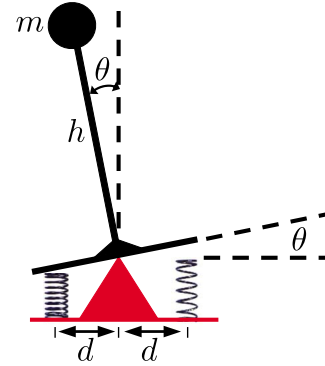


FIG. 9. (Color online) One DOF model for the wobble chair. In the simplified model the angle between the seat and the torso is fixed and control is applied at the base. This is an approximation to more complex system where torso flexion causes rear spring compression and extension causes front spring compression for effective base applied control.

These constraints effectively reduce the system to a two-dimensional state space, which is a deterministic system plus noise.

**3. One segment, planar model**

The equation of motion for the inverted pendulum with stabilizing springs and limited gain control is calculated using Lagrange’s equations and written in first-order form,

$$\dot{\theta} = v, \tag{17}$$

$$\dot{v} = \frac{1}{mh^2}[(mgh - kd^2)\sin \theta - C(\theta, v) + N(t)],$$

where  $m$ ,  $g$ ,  $h$ ,  $\theta$ ,  $v$ ,  $k$ , and  $d$  are the mass, acceleration of gravity, height, rotation angle, angular velocity, spring stiffness, and the distance of the springs from the central ball joint, respectively. System noise  $N(t)$  is a zero mean Gaussian random function. The equation for the limited gain proportional-derivative control  $C$  is given by

$$C(\theta, v) = G_d v + \begin{cases} G_p \theta & \text{if } |\theta| < \theta_{cr} \\ \tau_{pmax} & \text{otherwise,} \end{cases} \tag{18}$$

where  $G_d$  is the derivative gain constant,  $\theta_{cr} = \tau_{pmax} / G_p$  is the smallest angle at which the maximum gain is achieved,  $G_p$  is the proportional gain constant, and  $\tau_{pmax}$  is the maximum torque producible by proportional gain. Physiologically, a limited gain controller represents the limited muscle strength of the abdominal and spinal extensor muscles. Noise  $N(t)$  is introduced into the physical system from muscle twitches, inaccurate motor unit activation, involuntary movements, or external environmental forces. It is simulated by a zero mean Gaussian normal distribution with a standard deviation equal to a given percentage of the gravitational term ( $mgh$ ). A noise frequency of 20 Hz is selected such that it substantially exceeds the frequency of small oscillations of system (17) about the inverted equilibrium ( $\approx 3$  Hz). We use realistic physical parameters typical of participants performing tests on the wobble chair (Table I).

TABLE I. Parameter table for one DOF model.

Parameter	Value	Source
$m$	69 kg	Typical subject
$g$	9.81 m/s <sup>2</sup>	Physical constant
$h$	43.0 cm	Typical subject
$k$	10 900 N/m	Wobble chair
$d$	10.35 cm	Value to generate 40% $mgh$
$G_d$	1 N m/(rad/s)	Calibration parameter
$G_p$	190 N m/rad	Calibration parameter
$\tau_{pmax}$	14.5 N m	Calibration parameter

**4. Dynamical boundaries for full and partial sampling with varying amounts of noise**

Ultimately we want a technique that extracts dynamical boundaries from experimental trials that only sample a small

portion of phase space. But for comparison, we first consider dynamical boundaries with full sampling. We look at the sensitivity on a regular grid (200×200) of points in phase space centered around the origin with a range of ±15° × ±15°/s (we use degrees instead of radians for plotting and visualization purposes). Each of these points is taken as an initial condition to determine the flow map over a fixed horizon time  $T$  directly from the vector field (17). The FTLE is calculated for each point on the interior of the grid based on the expansion of the state transition matrix. These results are combined over state space to produce a FTLE field. The FTLE field was first calculated by flowing time forward  $T=3$  s.

In Fig. 10, we show the FTLE field and extracted boundaries for a no-noise case and several cases of increasing noise (1%, 2%, and 5%). From the extracted boundaries, we cal-

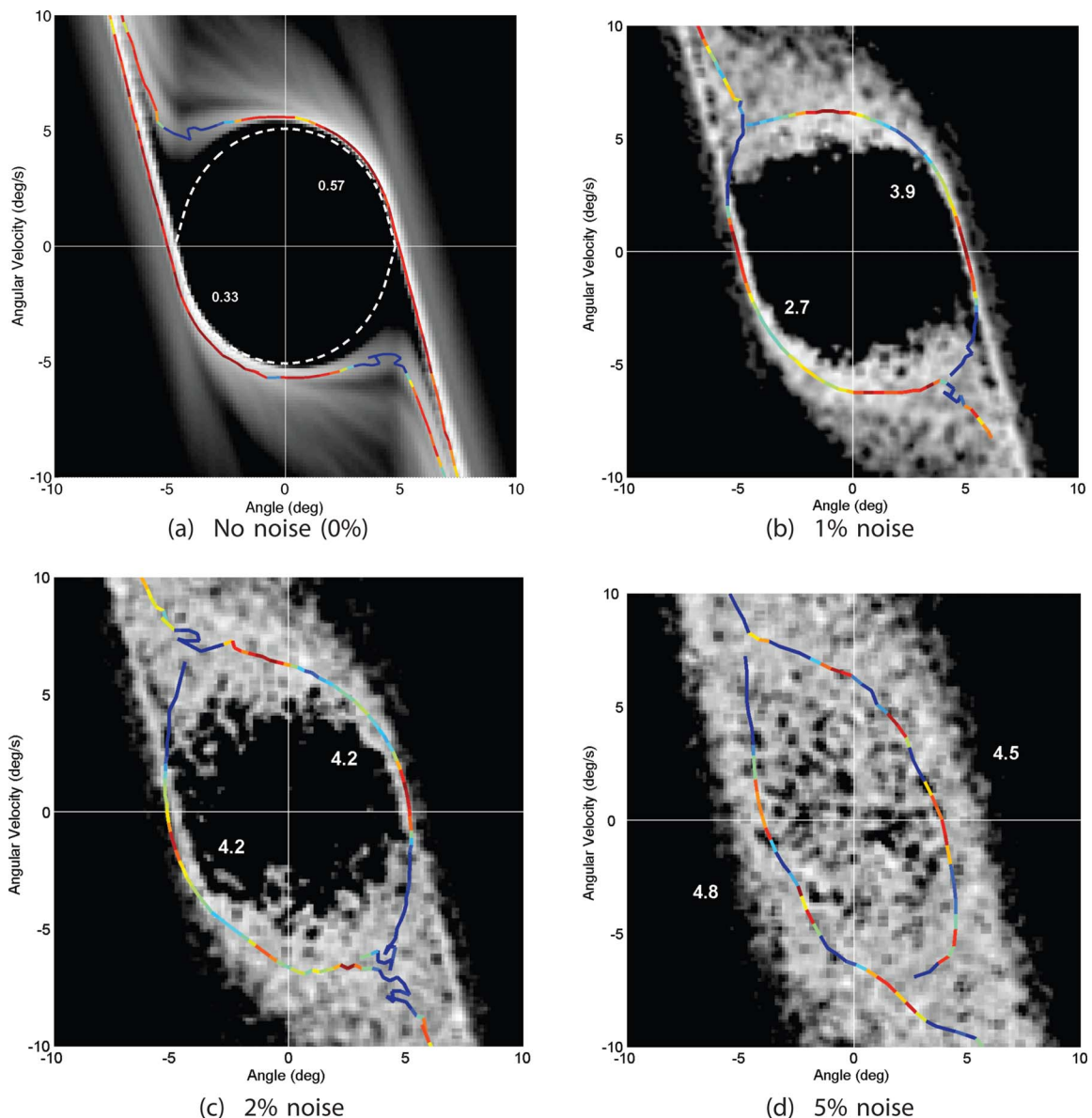


FIG. 10. (Color online) The FTLE field and detected boundaries (ridges) are shown for a full sampling of phase space for the reduced order wobble chair model at four values of the noise. The boundary separating the stable and unstable regions of phase space is shown. The boundary has two parts (roughly an upper and a lower part), and we give the average flux across each. Each boundary is made up of elements color coded according to the amount of flux across the element: low flux (higher strength) is lighter, high flux (lower strength) is darker. The solid closed curve in (a) is the theoretical boundary for zero noise.

TABLE II. Areas and flux of the basin of stability.

Noise level	Area (deg <sup>2</sup> /s)	Flux
Analytical	73	0
0%	100	0.45
1%	107	3.4
2%	113	4.2
5%	91	4.7
10%	0	...

culate the area of the basin of stability as well as the average flux across the boundary. The results are in Table II. The dashed closed curve in Fig. 10(a) is the analytically computed boundary for zero noise, which corresponds to a heteroclinic cycle between the two saddle points in the phase space.

Random noise slightly perturbs the trajectories as they evolve making the system no longer deterministic. This has the potential to have a dramatic effect on the future of a trajectory. Trajectories near the separatrix may be perturbed to the opposite side crossing the barrier. Thus, stable trajectories may become unstable and unstable trajectories may become stable. However, a separatrix still exists despite the presence of noise. We also considered a noise level of 10%, but no stable region could be defined. Only one separatrix was found, going from the upper left to lower right, continuing the trend of Fig. 10.

To give us an idea of what a realistic partial sampling of the phase space would yield, we considered the following. Experimental trials on the wobble chair start from rest (at the origin) and are driven by random force perturbations which tend to have a destabilizing effect, eventually resulting in a fall. We considered 20 such independent trials, beginning at the origin, lasting for 30 s. These simulated trials produce time-series data, shown overlaid in Fig. 11(a). The noise level was set at 1%. These trials are transformed into trajectories in an appropriate state space [Fig. 11(b)] via reconstruction, as described in Sec. II.

This set of trajectories is used to produce a FTLE field shown in Fig. 12(a). Unlike the full sampling of Fig. 10, the simulated experimental data only contain information about the portion of state space where the trajectories have explored. Since the forward dynamic simulation begins at the phase space origin and is randomly perturbed from this location, only trajectories that are initially stable and may become unstable are included. Despite being less complete than boundaries generated from full grid data, the portion of the boundary which is sampled is in the same general location, as shown by the comparison in Fig. 12(b). This provides confidence that partial sampling of the phase space using experimental trials can be used to detect the boundaries as well as estimate the differential and average flux across it.

We note that although 20 independent trials were used for clarity of illustration, separate work<sup>58</sup> indicates that portions of the recovery envelope structure may be identified with very few trials using this method. This is critical from the point of view of experiments where tests are limited or expensive, e.g., the number of falling trials is limited for a given individual. A part of future work will be to determine the number of experimental trials necessary to reveal the desired level of dynamical structural detail.

### C. Two degree of freedom model

A two DOF model has been developed for the two segment planar wobble chair. This model better represents the true motion of unstable sitting by treating the lower body as one segment, the upper body as another, and the lumbar spine (L4-L5) as the joint, as shown Fig. 13(a). A planar system is used to reduce the complexity of the results while still capturing most of the nonlinear behavior. The system is modeled as a double inverted pendulum, with a two-dimensional configuration variable  $\theta = (\theta_1, \theta_2)$  of the segment angles, measured with respect to a fixed inertial frame and increasing counterclockwise, i.e.,  $\theta_1$  is measured from the horizontal and  $\theta_2$  from the vertical [Fig. 13(b)]. Notice that the configuration space is the two-torus  $\mathbb{T}^2$  and the phase space is  $\mathbb{T}^2 \times \mathbb{R}^2$ , or alternatively, two copies of the tangent bundle of the circle,  $TS^1 \times TS^1$ . Since we are concerned with relatively small motions in the angular configuration variables, for purposes of FTLE computation we treat the phase space as Euclidean  $\mathbb{R}^4$ .

A control torque is applied between the two segments bringing the body into flexion or extension. During flexion, the lower segment rises in the front and the upper segment bends forward toward the feet. During extension, the lower segment drops in the front and the upper segment bends back away from the feet. Through these dynamic motions the combined COM of the body only shifts slightly, but the seat angle changes. When in flexion, the seat is rotated clockwise increasing the restorative moment of the rear spring providing a torque that accelerates the COM forward. The reverse occurs during extension. Thus, active control of the lumbar spine has the effect of controlling movement at the base of the double inverted pendulum. Furthermore, the dynamic movements of the segments have an effect on the motion via inertial coupling terms.<sup>41,55</sup>

#### 1. Two segment, planar model

The equation of motion for the planar double inverted pendulum with stabilizing springs and limited gain control is calculated using the Lagrangian formulation yielding

$$M(\theta)\ddot{\theta} + C(\theta, \dot{\theta})\dot{\theta} + G(\theta) = \tau(\theta, \dot{\theta}), \quad (19)$$

where  $M$  is the (uniformly positive definite) inertia tensor,  $C$  contains the velocity-dependent terms,  $G$  contains the effects of gravity, and  $\tau = (\tau_1, \tau_2)$  is the torque applied at the segment joints. The analysis given elsewhere<sup>59</sup> yields the matrices  $M$ ,  $C$ , and  $G$  as

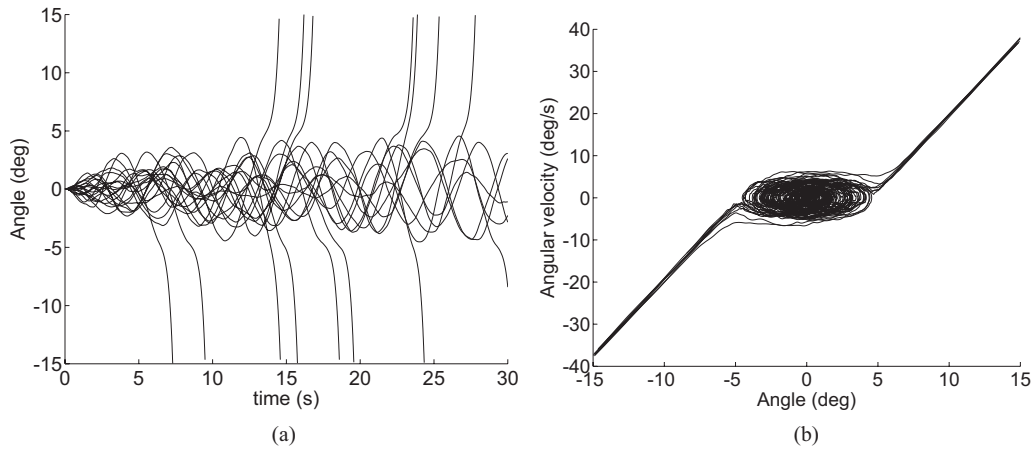


FIG. 11. A time-series data set generated from 20 simulated experimental trials. (a) Time plot shows each trial beginning from the state space origin. (b) The trials shown as trajectories in phase space.

$$M(\boldsymbol{\theta}) = \begin{bmatrix} m_1 \|\mathbf{c}_1\|^2 + m_2 \|\mathbf{L}_1\|^2 + I_1 & m_2 (R'(\theta_1) \mathbf{L}_1) \cdot (R'(\theta_2) \mathbf{c}_2) \\ m_2 (R'(\theta_1) \mathbf{L}_1) \cdot (R'(\theta_2) \mathbf{c}_2) & m_2 \|\mathbf{c}_2\|^2 + I_2 \end{bmatrix},$$

$$C(\boldsymbol{\theta}, \dot{\boldsymbol{\theta}}) = \begin{bmatrix} 0 & m_2 (R'(\theta_1) \mathbf{L}_1) \cdot (R''(\theta_2) \mathbf{c}_2) \dot{\theta}_2 \\ m_2 (R''(\theta_1) \mathbf{L}_1) \cdot (R'(\theta_2) \mathbf{c}_2) \dot{\theta}_1 & 0 \end{bmatrix}, \tag{20}$$

$$G(\boldsymbol{\theta}) = \begin{bmatrix} m_1 \mathbf{g} \cdot (R'(\theta_1) \mathbf{c}_1) + m_2 \mathbf{g} \cdot (R'(\theta_1) \mathbf{L}_1) \\ m_2 \mathbf{g} \cdot (R'(\theta_2) \mathbf{c}_2) \end{bmatrix},$$

where  $m_i$  is the mass of segment  $i$ ,  $\mathbf{c}_i$  is the vector from joint  $i$  to the segment  $i$  COM,  $\mathbf{L}_1$  is the vector from joint 1 to joint 2,  $I_i$  is the moment of inertia of segment  $i$  about its COM,  $\mathbf{g}=(0, -g)$  is the gravitational acceleration, the torque is given by

$$\boldsymbol{\tau}(\boldsymbol{\theta}, \dot{\boldsymbol{\theta}}) = \begin{bmatrix} \tau_{spr} - (\tau_{sk} + \tau_{sd} + C_{PD}) \\ \tau_{sk} + \tau_{sd} + C_{PD} \end{bmatrix} = \begin{bmatrix} k_1 d^2 \sin \theta_1 - (k_2(\theta_2 - \theta_1) + k_3(\dot{\theta}_2 - \dot{\theta}_1) + C_{PD}(\theta_1, \theta_2, \dot{\theta}_1, \dot{\theta}_2)) \\ k_2(\theta_2 - \theta_1) + k_3(\dot{\theta}_2 - \dot{\theta}_1) + C_{PD}(\theta_1, \theta_2, \dot{\theta}_1, \dot{\theta}_2) \end{bmatrix}, \tag{21}$$

the proportional-derivative control is similar to the one DOF system (18),

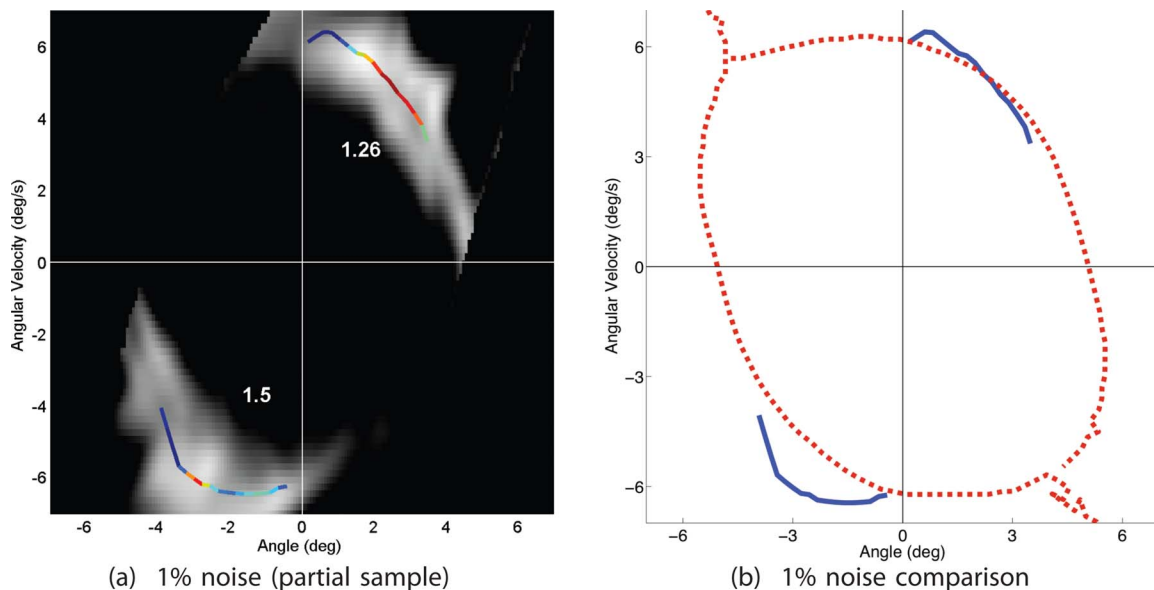


FIG. 12. (Color online) (a) A portion of a dynamical boundary found by analyzing the FTLE field resulting from the trajectories of Fig. 11. Only portions of the complete boundary are accessible by this method. The flux for the upper-right and lower-left portions is also shown. (b) A comparison of the dynamical boundaries from the partial sample (solid) and full-grid data (dotted).

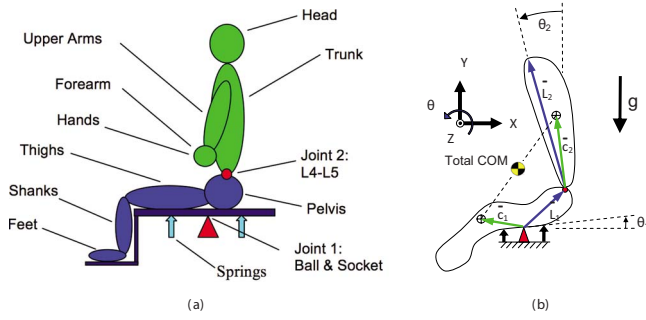


FIG. 13. (Color online) (a) Model of a person sitting on the wobble chair. Components of the lower body contribute to segment one, while components of the upper body make up segment two. (b) Simplified model of a person sitting on the wobble chair. Vectors  $c_i$  are from joint  $i$  to the COM of segment  $i$ , while  $L_i$  is the vector from joint 1 to joint 2. The deflection of the lower body and seat from the balanced configuration is  $\theta_1$  and the deflection of the upper body from the vertical position is  $\theta_2$ . Forces are applied to the stabilizing springs providing effective base control of the combined COM as the body pivots at the lumbar spine (L4-L5) during flexion and extension of the torso.

$$C_{PD}(\theta_1, \theta_2, \dot{\theta}_1, \dot{\theta}_2) = G_d \dot{\theta}_{COM} + \begin{cases} G_p \theta_{COM} & \text{if } |\theta_{COM}| < \theta_{cr} \\ \tau_{pmax} & \text{otherwise,} \end{cases} \quad (22)$$

where  $\theta_{COM}$  is the deviation from vertical of the total COM with respect to the seat pivot,

$$\theta_{COM} = -\arctan\left(\frac{c_{COMx}}{c_{COMy}}\right), \quad (23)$$

$$c_{COM} = \frac{m_1 R(\theta_1) c_1 + m_2 (R(\theta_1) L_1 + R(\theta_2) c_2)}{m_1 + m_2},$$

and the rotation matrices  $R(\theta_i)$  are given by

$$R(\theta_i) = \begin{bmatrix} \cos \theta_i & -\sin \theta_i \\ \sin \theta_i & \cos \theta_i \end{bmatrix}, \quad (24)$$

where a prime denotes differentiation of the matrix with respect to its argument. The kinematic and dynamic parameters used for the simulation are given in Table III. The anthropometric data are from Ref. 8.

Like the previous models, the system was driven by zero mean Gaussian random force perturbations with a standard deviation equal to 1% of the gravitational term.

### 2. Portions of the basin of stability boundaries in two DOFS

The FTLE field was generated using forward dynamics simulations for a horizon time  $T=0.5$  s based on a regular grid of initial conditions (Fig. 14). Since the LCS is a 3D surface separating the four-dimensional (4D) phase space into two distinct regions (stable and unstable), it is easier to view planar sections of state space rather than the entire 4D hypervolume. We verified that the LCS bounds the basin of stability by comparing with a “brute-force” measure of stability: we have marked with + those initial conditions which cross a distant boundary in the unstable region (reaching large angles of  $|\theta_1|=300^\circ$  or  $|\theta_2|=300^\circ$  within 30 s). The remaining presumably stable initial conditions are marked with circles. The stable trajectories generally aligned with the valley in the FTLE field and are well within the basin of stability boundaries as delimited by the LCS.

### D. Determining the basin of stability through wobble chair experiments

The goal of the methods outlined in this paper is to detect dynamical boundaries from actual experimental data. Since we were successfully able to obtain a basin of stability from simulated experimental time series, as just described, we conducted some preliminary experiments on eight human participants on a wobble chair in the laboratory, with the goal of identifying the human torso basin of stability from seated stability test data.<sup>59,61</sup>

For the experiments, wobble chair motion was constrained to the sagittal plane and two DOFs were measured within that plane as a function of time (fore-aft movement of the lower and upper body segments). With the rates calculated, we had trajectories in a 4D state space. Using the above procedure, but scaled to four dimensions, we were able to measure the basin of stability by detecting the region enclosed by the 3D recovery envelope. Eight participants were tested, and the measured 4D volume of the basin of stability ranged from 252 to 5760  $\text{deg}^4/\text{s}^2$  with a mean (standard deviation) of 2190 (1760)  $\text{deg}^4/\text{s}^2$ .

These results demonstrate that a basin of stability can be generated from time series data collected from musculoskeletal biomechanics experiments. Further analyses of the basin of stability, along the lines of the risk assessment mentioned in Sec. I, are left as future work. Our modest goal is that the ability to measure the basin of stability may serve as an additional useful tool to evaluate other balance control problems for which time series data are available.

TABLE III. Parameter table for two DOF model.

Parameter	Value	Source/description
$m_1$	27.4 kg	Lower body mass
$m_2$	31.8 kg	Upper body mass
$I_1$	2.35 $\text{kg m}^2$	Lower body mass moment of inertia
$I_2$	4.86 $\text{kg m}^2$	Upper body mass moment of inertia
$L_{1x}$	0.1272 m	Lower body segment vector—horizontal
$L_{1y}$	0.1580 m	Lower body segment vector—vertical
$L_{2x}$	0.000 m	Upper body segment vector—horizontal
$L_{2y}$	0.7179 m	Upper body segment vector—vertical
$c_{1x}$	-0.1771 m	Lower body COM vector horizontal
$c_{1y}$	0.0780 m	Lower body COM vector vertical
$c_{2x}$	0.000 m	Upper body COM vector horizontal
$c_{2y}$	0.2736 m	Upper body COM vector vertical
$g$	9.81 $\text{m/s}^2$	Acceleration of gravity
$k_1$	10 900 N/m	Wobble chair linear spring constant
$d$	10.35 cm	Distance from ball joint to springs
$k_2$	100 N m	Torsional stiffness of the spine
$k_3$	0.1 N m s	Torsional damping of the spine
$G_d$	200 N m/(rad/s)	Derivative gain
$G_p$	$3 \times 10^5$ N m/rad	Proportional gain
$\tau_{pmax}$	$8 \times 10^4$ N m	Maximum proportional gain

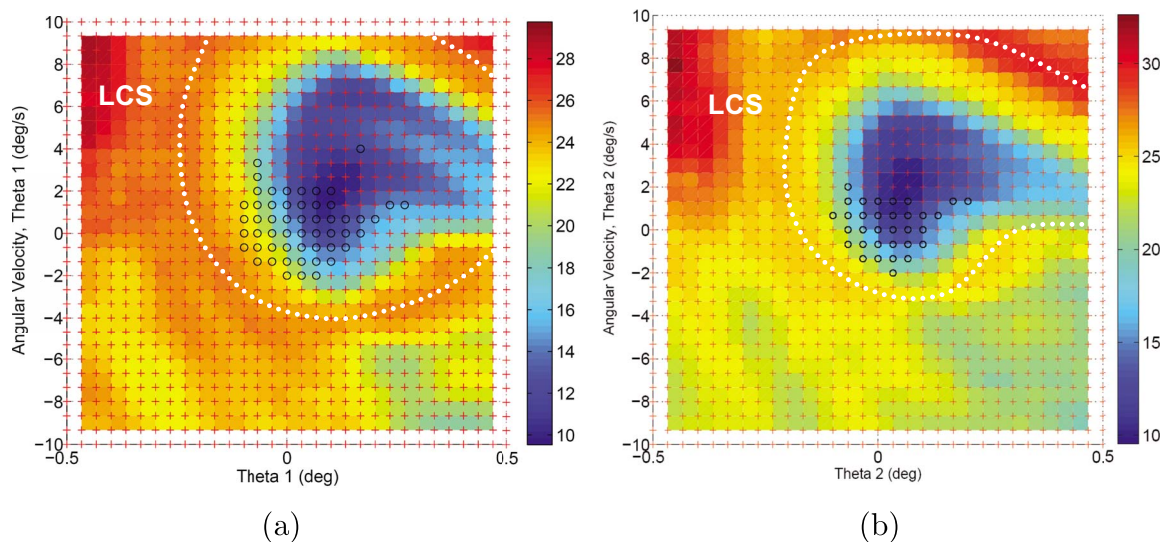


FIG. 14. (Color online) Recovery envelopes and basin of stability from 4D simulated data. FTLE field for simulated wobble chair data seen in two different two-dimensional slices of the full 4D state space (the slice is at the origin in the two other dimensions): (a)  $(\theta_1, \dot{\theta}_1)$  and (b)  $(\theta_2, \dot{\theta}_2)$ . Notice the ridge of high FTLE surrounding a region of low FTLE. This ridge is a slice of a LCS, a recovery envelope which bounds—and from which we can measure the size of—the basin of stability. Although only two dimensions are shown for visualization purposes, the basin volume can be computed in the full 4D state space.

#### IV. CONCLUSIONS AND FUTURE WORK

The extension of separatrix methods to experimental time series analysis of mechanical and biomechanical systems provides better means of comparison to analytical models and gives greater insight into possible—but as yet unobserved—behaviors based on the determined phase space structure and interconnectivity. Furthermore, detection of separatrices dividing regions of failure from regions of safety will provide new robust stability measures that provide additional information over what is currently available. The methods described herein apply to other areas where nonlinear time series analysis is used to analyze not only mechanical systems but also nonmechanical systems, such as meteorological, financial, psychological, and population observations. Whereas previous research in time series analysis using FTLEs has focused only on determining whether the dynamics comes from deterministic chaos or noise, we have shown that there may be more information to be mined from the data. Structure within the underlying deterministic system may yield information about phase-space transport phenomena that is critical to understanding the behavior of the system.

##### A. Recovery envelopes: A new tool in the evaluation of fall risk?

In biomechanics, determining dynamical boundaries will be useful in understanding how our neuromuscular reflexes and the nonlinear behavior of our musculoskeletal system contribute to stability maintenance during walking and more general motor control. The identification of these boundaries will contribute to new procedures using available data to prevent, diagnose, and treat medical problems. Case in point, dynamical boundaries may provide robust biomechanical measures of the risk of falling for a given individual and/or load-carrying task. We have speculated that an individual's fall risk can be accurately measured by how close his or her

state space trajectory comes to the recovery envelope, as shown schematically in Fig. 4. But future experiments are needed to test this hypothesis. Finally, we emphasize that the idea of the recovery envelope is not limited to evaluating fall risk and could have broader impact if applied to other areas of health and safety where balance and recovery are involved.

- <sup>1</sup>Aldridge, B. B., Haller, G., Sorger, P. K., and Lauffenburger, D. A., "Direct Lyapunov exponent analysis enables parametric study of transient signaling governing cell behaviour." *IEE Proc.-Syst. Biol.* **153**, 425–432 (2006).
- <sup>2</sup>Bottaro, A., Casadio, M., Morasso, P. G., and Sanguineti, V., "Body sway during quiet standing: Is it the residual chattering of an intermittent stabilization process?," *Hum. Mov. Sci.* **24**, 588–615 (2005).
- <sup>3</sup>Bureau of Labor Statistics, 2001, United States Department of Labor, <http://www.bls.gov/iif/oshcdnew.htm>.
- <sup>4</sup>Casdagli, M., Eubank, S., Farmer, J. D., and Gibson, J., "State space reconstruction in the presence of noise," *Physica D* **51**, 52–98 (1991).
- <sup>5</sup>Cholewicki, J. and McGill, S., "Mechanical stability of the in vivo lumbar spine: Implications for injury and chronic low back pain," *Clin. Biomech. (Bristol, Avon)* **11**, 1–15 (1996).
- <sup>6</sup>Cholewicki, J., Polzhofer, G. K., and Radebold, A., "Postural control of trunk during unstable sitting," *J. Biomech.* **33**, 1733–1737 (2000).
- <sup>7</sup>Davidson, B. S., "Experimental and simulation-based assessment of the human postural response to sagittal plane perturbations with localized muscle fatigue and aging," Ph.D. thesis, Virginia Tech-Wake Forest University School of Biomedical Engineering and Science, 2007.
- <sup>8</sup>De Leva, P., "Adjustments to Zatsiorsky-Seluyanov's segment inertia parameters," *J. Biomech.* **29**, 1223–1230 (1996).
- <sup>9</sup>Dellnitz, M., Junge, O., Koon, W. S., Lekien, F., Lo, M. W., Marsden, J. E., Padberg, K., Preis, R., Ross, S. D., and Thiere, B., "Transport in dynamical astronomy and multibody problems," *Int. J. Bifurcation Chaos Appl. Sci. Eng.* **15**, 699–727 (2005).
- <sup>10</sup>Dellnitz, M., Junge, O., Lo, M. W., Marsden, J. E., Padberg, K., Preis, R., Ross, S. D., and Thiere, B., "Transport of Mars-crossing asteroids from the quasi-Hilda region," *Phys. Rev. Lett.* **94**, 231102 (2005).
- <sup>11</sup>Dingwell, J. B., "Lyapunov exponent," in *The Wiley Encyclopedia of Biomedical Engineering*, edited by Akay, M. (Wiley, New York, 2006).
- <sup>12</sup>Dingwell, J. B. and Cusumano, J. P., "Nonlinear time series analysis of normal and pathological human walking," *Chaos* **10**, 848–863 (2000).
- <sup>13</sup>El Rifai, K., Haller, G., and Bajaj, A., "Global dynamics of an autoparametric spring-mass-pendulum system," *Nonlinear Dyn.* **49**, 105–116 (2007).

- <sup>14</sup>Ellner, S. and Turchin, P., "Chaos in a noisy world: New methods and evidence from time-series analysis," *Am. Nat.* **145**, 343–375 (1995).
- <sup>15</sup>England, S. and Granata, K. P., "The influence of gait speed on local dynamic stability of walking," *Gait and Posture* **25**, 172–178 (2007).
- <sup>16</sup>Falconer, I., Gottwald, G. A., Melbourne, I., and Wormnes, K., "Application of the 0-1 test for chaos to experimental data," *SIAM J. Appl. Dyn. Syst.* **6**, 395–402 (2007).
- <sup>17</sup>Franca, L. F. P. and Savi, M. A., "Distinguishing periodic and chaotic time series obtained from an experimental nonlinear pendulum," *Nonlinear Dyn.* **26**, 255–273 (2001).
- <sup>18</sup>Fung, Y., *Biomechanics: Mechanical Properties of Living Tissues*, 2nd ed. (Springer-Verlag, Berlin, 1993).
- <sup>19</sup>Gabern, F., Koon, W. S., Marsden, J. E., and Ross, S. D., "Theory and computation of non-RRKM lifetime distributions and rates in chemical systems with three or more degrees of freedom," *Physica D* **211**, 391–406 (2005).
- <sup>20</sup>Gabern, F., Koon, W. S., Marsden, J. E., Ross, S. D., and Yano, T., "Application of tube dynamics to non-statistical reaction processes," *Few-Body Syst.* **38**, 167–172 (2006).
- <sup>21</sup>Gómez, G., Koon, W. S., Lo, M. W., Marsden, J. E., Masdemont, J., and Ross, S. D., "Connecting orbits and invariant manifolds in the spatial three-body problem," *Nonlinearity* **17**, 1571–1606 (2004).
- <sup>22</sup>Granata, K. and Orishimo, K., "Response of trunk muscle coactivation to changes in spinal stability," *J. Biomech.* **34**, 1117–1123 (2001).
- <sup>23</sup>Granata, K. P. and Lockhart, T. E., "Dynamic stability differences in fall-prone and healthy adults," *J. Electromyogr Kinesiol* **18**, 172–178 (2008).
- <sup>24</sup>Haller, G., "Finding finite-time invariant manifolds in two-dimensional velocity fields," *Chaos* **10**, 99–108 (2000).
- <sup>25</sup>Haller, G., "Distinguished material surfaces and coherent structures in 3D fluid flows," *Physica D* **149**, 248–277 (2001).
- <sup>26</sup>Haller, G., "Lagrangian structures and the rate of strain in a partition of two-dimensional turbulence," *Phys. Fluids* **13**, 3365–3385 (2001).
- <sup>27</sup>Haller, G., "Lagrangian coherent structures from approximate velocity data," *Phys. Fluids* **14**, 1851–1861 (2002).
- <sup>28</sup>Haller, G. and Yuan, G., "Lagrangian coherent structures and mixing in two-dimensional turbulence," *Physica D* **147**, 352–370 (2000).
- <sup>29</sup>Horak, F. and Nashner, L. M., "Central programming of postural movements: Adaptation to altered support-surface configurations," *J. Neurophysiol.* **55**, 1369–1381 (1986).
- <sup>30</sup>Iqbal, K. and Pai, Y., "Predicted region of stability for balance recovery: Motion at the knee joint can improve termination of forward movement," *J. Biomech.* **33**, 1619–1627 (2000).
- <sup>31</sup>Jaffé, C., Ross, S. D., Lo, M. W., Marsden, J. E., Farrelly, D., and Uzer, T., "Theory of asteroid escape rates," *Phys. Rev. Lett.* **89**, 011101 (2002).
- <sup>32</sup>Kantz, H. and Schreiber, T., *Nonlinear Time Series Analysis*, 2nd ed. (Cambridge University Press, Cambridge, 2004).
- <sup>33</sup>Kelsey, J. L. and White, A. A., "Epidemiology and impact of low-back pain," *Spine* **5**, 133–142 (1980).
- <sup>34</sup>Koon, W. S., Lo, M. W., Marsden, J. E., and Ross, S. D., "Heteroclinic connections between periodic orbits and resonance transitions in celestial mechanics," *Chaos* **10**, 427–469 (2000).
- <sup>35</sup>Kuo, A. and Zajac, F., "A biomechanical analysis of muscle strength as a limiting factor in standing posture," *J. Biomech.* **26**, 137–150 (1993).
- <sup>36</sup>Lee, H. and Granata, K. P., "Process stationarity and reliability of trunk postural stability," *Clin. Biomech. (Bristol, Avon)* **23**, 735–742 (2008).
- <sup>37</sup>Lekien, F. and Ross, S. D., "The computation of finite-time Lyapunov exponents on unstructured meshes and for non-Euclidean manifolds," *Chaos* **19**, 047504 (2009).
- <sup>38</sup>Lekien, F., Shadden, S. C., and Marsden, J. E., "Lagrangian coherent structures in  $n$ -dimensional systems," *J. Math. Phys.* **48**, 065404 (2007).
- <sup>39</sup>Mathur, M., Haller, G., Peacock, T., Ruppert-Felsot, J. E., and Swinney, H. L., "Uncovering the Lagrangian skeleton of turbulence," *Phys. Rev. Lett.* **98**, 144502 (2007).
- <sup>40</sup>Morasso, P. and Sanguineti, V., "Ankle muscle stiffness alone cannot stabilize balance during quiet standing," *J. Neurophysiol.* **88**, 2157–2162 (2002).
- <sup>41</sup>Murray, R. and Hauser, J., *A Case Study in Approximate Linearization: The Acrobot Example* (University of California, Berkeley, 1991), pp. 1–43.
- <sup>42</sup>Norris, J. A., Marsh, A. P., Granata, K. P., and Ross, S. D., "Positive feedback in powered exoskeletons: Improved metabolic efficiency at the cost of reduced stability?," ASME International Design Engineering Technical Conference and Computers and Information in Engineering Conference, Las Vegas, NV, 2007.
- <sup>43</sup>Norris, J. A., Marsh, A. P., Granata, K. P., and Ross, S. D., "Revisiting stability of 2D passive biped walking: Local behavior," *Physica D* **237**, 3038–3045 (2008).
- <sup>44</sup>Packard, N., Crutchfield, J., Farmer, J., and Shaw, R., "Geometry from a time series," *Phys. Rev. Lett.* **45**, 712–716 (1980).
- <sup>45</sup>Pai, Y. and Patton, J., "Center of mass velocity-position predictions for balance control," *J. Biomech.* **30**, 347–354 (1997).
- <sup>46</sup>Parker, T. S. and Chua, L. O., *Practical Numerical Algorithms for Chaotic Systems* (Springer-Verlag, Berlin, 1989).
- <sup>47</sup>Peterka, R. J., "Postural control model interpretation of stabilogram diffusion analysis," *Biol. Cybern.* **82**, 335–343 (2000).
- <sup>48</sup>Poon, C.-S. and Barahona, M., "Titration of chaos with added noise," *Proc. Natl. Acad. Sci. U.S.A.* **98**, 7107–7112 (2001).
- <sup>49</sup>Reeves, N. P., Cholewicki, J., and Milner, T. E., "Muscle reflex classification of low-back pain," *J. Electromyogr Kinesiol* **15**, 53–60 (2005).
- <sup>50</sup>Rosenstein, M. T., Collins, J. J., and De Luca, C. J., "A practical method for calculating largest Lyapunov exponents from small data sets," *Physica D* **65**, 117–134 (1993).
- <sup>51</sup>Senatore, C. and Ross, S. D., "Detection and characterization of transport barriers in complex flows via ridge extraction of the finite time Lyapunov exponent field" (submitted).
- <sup>52</sup>Shadden, S. C., Lekien, F., and Marsden, J. E., "Definition and properties of Lagrangian coherent structures: Mixing and transport in two-dimensional aperiodic flows," *Physica D* **212**, 271–304 (2005).
- <sup>53</sup>Shadden, S. C. and Taylor, C. A., "Characterization of coherent structures in the cardiovascular system," *Ann. Biomed. Eng.* **36**, 1152–1162 (2008).
- <sup>54</sup>Slota, G. P., Granata, K. P., and Madigan, M. L., "Effects of seated whole-body vibration on postural control of the trunk during unstable seated balance," *Clin. Biomech. (Bristol, Avon)* **23**, 381–386 (2008).
- <sup>55</sup>Spong, M. W., "The swing up control problem for the Acrobot," *IEEE Control Syst. Mag.* **15**, 49–55 (1995).
- <sup>56</sup>Strang, G., *Linear Algebra and Its Applications*, 3rd ed. (Harcourt Brace Jovanovich, San Diego, 1988).
- <sup>57</sup>Tallapragada, P. and Ross, S., "Particle segregation by Stokes number for small neutrally buoyant spheres in a fluid," *Phys. Rev. E* **78**, 036308 (2008).
- <sup>58</sup>Tanaka, M. and Ross, S. D., "Separatrices and basins of stability from time series data: An application to biodynamics," *Nonlinear Dyn.* **58**, 1–21 (2009).
- <sup>59</sup>Tanaka, M. L., "Biodynamic analysis of human torso stability using finite time Lyapunov exponents," Ph.D. thesis, Virginia Tech-Wake Forest University School of Biomedical Engineering and Science, 2008.
- <sup>60</sup>Tanaka, M. L. and Granata, K., "Methods & nonlinear analysis for measuring torso stability," ASCE 18th Engineering Mechanics Division Conference, Blacksburg, VA, 3–6 June 2007.
- <sup>61</sup>Tanaka, M. L., Nussbaum, M. A., and Ross, S. D., "Evaluation of the threshold of stability for the human spine," *J. Biomech.* **42**, 1017–1022 (2009).
- <sup>62</sup>Truesdell, C. and Noll, W., *The Non-Linear Field Theories of Mechanics*, 3rd ed. (Springer-Verlag, Berlin, 2004).
- <sup>63</sup>Vukobratović, M. and Borovac, B., "Zero-moment point—Thirty five years of its life," *Int. J. Humanoid Rob.* **1**, 157–173 (2004).
- <sup>64</sup>Vukobratović, M. and Juricic, D., "Contribution to the synthesis of biped gait," *IEEE Trans. Biomed. Eng.* **16**, 1–6 (1969).
- <sup>65</sup>Wiggins, S., *Chaotic Transport in Dynamical Systems*, Interdisciplinary Applied Mathematics Vol. 2 (Springer, New York, 1992).
- <sup>66</sup>Wiggins, S., *Introduction to Applied Nonlinear Dynamical Systems and Chaos*, Texts in Applied Mathematics Science Vol. 2, 2nd ed. (Springer-Verlag, Berlin, 2003).
- <sup>67</sup>Winter, D., Patla, A., Rietydyk, S., and Ishac, M., "Ankle muscle stiffness in the control of balance during quiet standing," *J. Neurophysiol.* **85**, 2630–2633 (2001).
- <sup>68</sup>Winter, D. A., *Biomechanics and Motor Control of Human Movement* (Wiley, New York, 1990).
- <sup>69</sup>Wolf, A., Swift, J. B., Swinney, H. L., and Vastano, J. A., "Determining Lyapunov exponents from a time series," *Physica D* **16**, 285–317 (1985).
- <sup>70</sup>Yang, F., Anderson, F. C., and Pai, Y. C., "Predicted threshold against backward balance loss in gait," *J. Biomech.* **40**, 804–811 (2007).
- <sup>71</sup>Yang, F., Espy, D., and Pai, Y. C., "Feasible stability region in the frontal plane during human gait," *Ann. Biomed. Eng.* **37**, 2606–2614 (2009).
- <sup>72</sup>Yang, F., Passariello, F., and Pai, Y. C., "Determination of instantaneous stability against backward balance loss: Two computational approaches," *J. Biomech.* **41**, 1818–1822 (2008).